Article

Photoresponsive Activity of the $Zn_{0.94}Er_{0.02}Cr_{0.04}O$ Compound with Hemisphere-like Structure Obtained by Co-Precipitation

Robson França [1], Francisca Pereira Araujo [1], Luan Neves [2], Arthur Melo [2], Alexsandro Lins [1], Adriano Santana Soares [3], Josy Anteveli Osajima [3], Yuset Guerra [4], Luciano Costa Almeida [5] and Ramón Raudel Peña-Garcia [1,2,3,*]

[1] Programa de Pós-Graduação em Engenharia Física, Unidade Acadêmica do Cabo de Santo Agostinho, Universidade Federal Rural de Pernambuco, Cabo de Santo Agostinho 52171-900, PE, Brazil

[2] Unidade Acadêmica do Cabo de Santo Agostinho, Universidade Federal Rural de Pernambuco, Cabo de Santo Agostinho 52171-900, PE, Brazil

[3] Programa de Pós-Graduação em Ciências e Engenharia dos Materiais, Universidade Federal de Piauí, Teresina 64049-550, PI, Brazil

[4] Departamento de Física, Universidade Federal do Piauí, Teresina 64049-550, PI, Brazil

[5] Departamento de Engenharia Química, Universidade Federal de Pernambuco, Recife 50670-901, PE, Brazil

* Correspondence: raudel@ufpi.edu.br or ramon.raudel@ufrpe.br

Abstract: In this work, a ZnO hemisphere-like structure co-doped with Er and Cr was obtained by the co-precipitation method for photocatalytic applications. The dopant's effect on the ZnO lattice was investigated using X-ray diffraction, Raman, photoluminescence, UV-Vis and scanning electron microscopy/energy dispersive spectroscopy techniques. The photocatalytic response of the material was analyzed using methylene blue (MB) as the model pollutant under UV irradiation. The wurtzite structure of the $Zn_{0.94}Er_{0.02}Cr_{0.04}O$ compound presented distortions in the lattice due to the difference between the ionic radii of the Cr^{3+}, Er^{3+} and Zn^{2+} cations. Oxygen vacancy defects were predominant, and the energy competition of the dopants interfered in the band gap energy of the material. In the photocatalytic test, the MB degradation rate was 42.3%. However, using optimized H_2O_2 concentration, the dye removal capacity reached 90.1%. Inhibitor tests showed that •OH radicals were the main species involved in MB degradation that occurred without the formation of toxic intermediates, as demonstrated in the ecotoxicity assays in *Artemia salina*. In short, the co-doping with Er and Cr proved to be an efficient strategy to obtain new materials for environmental remediation.

Keywords: ZnO; rare-earth; transition metal; hemisphere-like structure; photocatalysis

1. Introduction

The population growth and increased demand for consumer goods, associated with inefficient waste management, have led to the accumulation of pollutants in water resources [1]. This is very worrying because recent research estimates that by 2050 around 65% of Earth's population will face a shortage of drinking water [2]. Among the anthropic activities that generate waste, intense industrial activity has stood out for releasing recalcitrant compounds, such as dyes and herbicides, which pose risks to the ecosystem and human health [3,4]. These pollutants have complex carbon chains that are resistant to degradation by the environment and are difficult to remove in conventional water treatments [5].

Advanced oxidative processes (AOPs) can satisfactorily break down molecules of organic pollutants. The high efficiency of AOPs is related to the formation of oxygen radical species that are directly responsible for the degradation of the contaminant [6,7]. Heterogeneous photocatalysis is an example of promising AOPs because it is a simple, efficient and low-cost method and can be used to degrade different toxic compounds in

wastewater [5,8]. In this technique, a semiconductor is used which, upon interaction with light, destabilizes the target molecules. When the semiconductor absorbs radiation, the valence band electron jumps to the conduction band, generating an electron–hole pair. This pair is responsible for the formation of important oxygenated radicals, mainly hydroxyl radicals, which attack the pollutant molecule [9–11].

Zinc oxide (ZnO) is a semiconductor that has been investigated for water purification, due to its physical and chemical stability, non-toxicity high sensitivity and wide band gap [12–15]. However, the rapid recombination of the electron–hole pair in ZnO strongly influences the photocatalytic activity [16,17]. Studies have shown that the inclusion of metal ions into the ZnO crystalline structure can delay the recombination of the electron–hole pair and contribute to the photocatalytic activity of this material [17–20]. Different studies proved that ZnO doped with transition metal ions presents a satisfactory photocatalytic response in recalcitrant compounds. Some of these studies included the addition of metals such as Co [21], Ag [22], Ni [23], Cu [24] and Mn [25]. The Cr insertion in the ZnO matrix is not a complicated process due to the proximity of the ionic radii of Cr^{3+} (0.62 Å) and Zn^{2+} (0.72 Å), and it can also be considered as an alternative to improve the photocatalytic response of ZnO. In general, Cr doping can promote the inhibition of the recombination of photogenerated electron–hole pairs [17]. In a classic photocatalysis experiment, Al Kalas et al. (2022) investigated the effect of different concentrations of Cr^{3+} ions on the structural, optical and photocatalytic properties of ZnO. The authors observed that the presence of the dopant in the ZnO lattice reinforced the oxygen defects that act directly to prevent the recombination of photogenerated charge carriers on the semiconductor surface. A better photocatalytic response was observed for the materials with low dopant concentrations [26]. Truong et al. (2019) also reported that Cr doping affected the band gap energy, expanding the semiconductor's energy absorption into the visible region. This resulted in a material that was efficient in removing the pollutant methyl orange [17].

There are also some studies that reported doping with rare earth metals as a strategy to increase the photocatalytic response of ZnO. Beyond increasing the lifetime of charge carriers in the valence and conduction bands, doping with these metals can also cause photoactivation with visible light [27–29]. Sowik et al. (2018) investigated the effect of different types of rare earth metal (Eu, Ho, Tb, Yb, Er and La) in the degradation of organic pollutants under UV-Vis irradiation. Among the materials obtained, the sample containing Er^{3+} ions demonstrated the highest efficiency of contaminant removal (almost 90%), due to effects such as the decrease in the band gap energy and recombination of the electron–hole pair [30]. Pascariu et al. (2019) also explored the effect of rare earths on the structural, optical and photocatalytic properties of ZnO nanostructures. According to this study, all materials presented a dye removal capacity above 60% within UV irradiation. However, Er^{3+} and Sm^{3+} dopants induced greater increases in the photocatalytic performance of ZnO [31].

Co-doping processes have been used as a new strategic approach to improve the photocatalytic capacity of semiconductor materials [32–34]. In this sense, the present work aimed to investigate the effect of Er^{3+} and Cr^{3+} cations' simultaneous addition on the structural, morphological and optical properties, as well as in the photocatalytic response of the ZnO hemisphere-like structure synthetized by co-precipitation. Specifically, we focused on the synthesis of the $Zn_{0.94}Er_{0.02}Cr_{0.04}O$ compound. The cations' concentration (2% of Er^{3+} and 4% of Cr^{3+}) in the ZnO host matrix was carefully determined to ensure that secondary phases were not formed. In addition, the photocatalytic response was investigated using the model pollutant methylene blue, a cationic dye that is resistant to biodegradation, representing risks to the ecosystem. Finally, the toxicity of the MB solution was investigated through ecotoxicity tests using *Artemia salina*.

2. Materials and Methods

2.1. Material Preparation

For the $Zn_{0.94}Er_{0.02}Cr_{0.04}O$ compound synthesis, the following reagents were used: zinc acetate (Aldrich, 98.0%, Barueri, Brazil), Erbium nitrate (Aldrich, 99.0%), Chromium nitrate (Aldrich, 99.0%) and distilled water as the solvent. Desired amounts of raw materials were weighed and dissolved in 100 mL of distilled water by magnetic stirring for 1 h. Then, the pH of the system was adjusted (pH = 9) by dropping a NaOH solution, and it was kept under constant stirring for 1 h until precipitate formation. The solid was washed five times with distilled water and then three times with ethanol. The material was dried at 100 °C (heating ramp 1 °C/min) for 6 h.

2.2. Characterization

The compound was characterized by X-ray diffraction (XRD) using an X-ray diffractometer, model D8 Advance from Bruker with Cu-Kα radiation (λ = 1.5406 Å), in the Bragg-Betano geometry. The Raman spectrum was measured with a Raman spectrometer, model Santerra from Bruker (Billerica, MA, USA), with an Olympus BX50 microscope coupled (Tokyo, Japan). The photoluminescence spectrum was measured in a Spectrofluorometer Horiba-JobinYvon Fluorolog-3 (Kyoto, Japan), while the diffuse reflectance spectra was obtained on a UV-Vis spectrometer, Shimadzu, UV-2700 (Kyoto, Japan). The spectra were deconvoluted using Gaussian fit. The morphology was obtained in a scanning electron microscope (SEM), and a TESCAN MIRA3 model (Brno, Czech Republic) with an energy dispersive X-ray spectrometer (EDS) coupled.

2.3. Photocatalytic Test

Photocatalytic tests were performed into a borosilicate reactor using a commercial lamp (160 W) as a source of UV radiation. In each of the tests, the photocatalyst concentration was 0.5 g·L^{-1} and methylene blue (MB) dye solution (1.0×10^{-5} mol·L^{-1}) was used as a model pollutant. The tests were performed at 25.0 ± 1.0 °C under magnetic stirring. The radiation intensity was monitored using a radiometer (Hanna). The adsorption equilibrium was reached in 30 min in the dark. Aliquots irradiated were removed during the test and centrifuged at $4400 \times g$ rpm for 45 s twice. The band at 664 nm was used to monitor the MB dye degradation using a spectrophotometer (Agilent Technologies, Cary 60 UV–Vis) in the range between 200 and 800 nm. The MB degradation was calculated by Equation (1).

$$Degradation(\%) = \frac{C_0 - C}{C_0} \times 100 \tag{1}$$

where C_0 and C correspond to the initial dye concentration and the final dye concentration (t = 150 min), respectively. The photocatalytic systems were also investigated using hydrogen peroxide (100 ppm) under optimal concentration [35]. To identify the roles of different reactive species, radical scavenger studies were performed using the ethylenediaminetetraacetic acid (EDTA) (2.4×10^{-6} mol L^{-1}), methyl alcohol (3.4×10^{-3} mol L^{-1}) and silver nitrate (5.0×10^{-4} mol L^{-1}), which are inhibitors of hole (h$^+$), hydroxyl radical ($^\bullet$OH) and electrons (e$^-$), respectively. The reusability of the material was tested for up to three consecutive cycles and the degradation rate determined in each case.

2.4. Ecotoxicity

The toxicity of the irradiated solution with photocatalyst material was analyzed using *Artemia salina* microcrustaceans. The nauplii were cultivated in a synthetic saline solution with constant illumination for 48 h. After this time, the nauplii were added to the solution containing MB dye-irradiated and synthetic saline solution (1:1 *v/v*). The survival rate of *Artemia salina* was evaluated after 24 h and 48 h [32].

3. Results and Discussion

3.1. Structural, Optical and Morphological Characterization

Figure 1 presents the X-ray diffraction pattern and Raman spectrum for the $Zn_{0.94}Er_{0.02}Cr_{0.04}O$ compound synthesized via co-precipitation. In Figure 1a, we can see that the compound presents diffraction peaks representative of the ZnO wurtzite structure with $P6_3mc$ space group, which are identified by the crystallographic card JCPDS No. 36-1451. In addition, there are two diffraction peaks at 2θ values of 33.5° and 59.5° marked with (@) which are indexed to the $Zn(OH)_2$ phase with data from the crystallographic card: JCPDS No. (38-0356). The secondary phase formation may be a consequence of the calcination temperature used in this study (100 °C for 6 h).
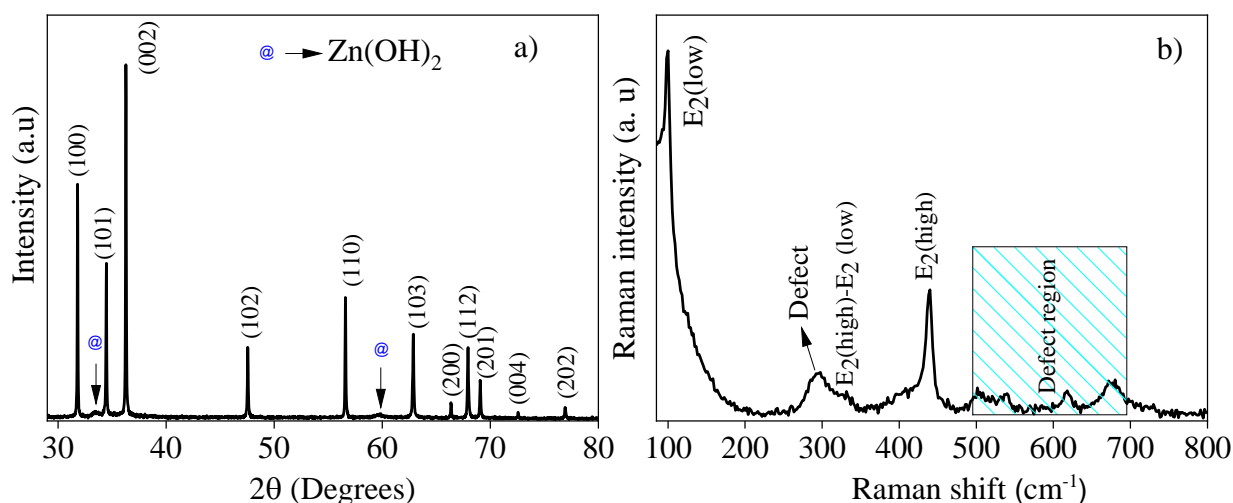

Figure 1. (**a**) X-ray diffraction pattern; (**b**) Raman spectrum for the $Zn_{0.94}Er_{0.02}Cr_{0.04}O$ compound.

The lattice parameters (*a* and *c*) are calculated using the equation that correlates the interplanar spacing, Miller indices and the lattice constants for the ZnO with hexagonal structure [36]. The calculated values for *a* and *c* are 3.2468(1) Å and 4.9482(3) Å, respectively, which are smaller than the recently reported values for ZnO [37]. This indicates that the dopants' insertion into the ZnO host lattice produces structural distortions that can be associated with the difference between the ionic radii of the dopant cations (Er^{3+} (0.89 Å) and Cr^{3+} (0.62 Å)) and the Zn^{2+} (0.74Å) host cations [38].

The Scherrer equation [36] was used to estimate the average crystallite size (D) and the value obtained was 86 nm. This result is four times higher than the value reported for ZnO nanostructures by Rocha et al. [37]. The Er and Cr ions' insertion in the ZnO structure can be classified as the donor's dopants because they have more of an oxidation state, if compared to the Zn ions. This difference can cause imperfections in the ZnO structure or attenuate the present interstitial defects; as defects are essential for structural changes, an increase in the average crystallite size could happen as Zn cations are replaced by Er and Cr cations. Furthermore, the energetic competition between the dopant cations, because they have different characteristics (ionic radii, electronegativity, etc.), may contribute to the nucleation and growth mechanisms, increasing the driving force that contributes to the crystallite's growth [36,39,40].

Figure 1b exhibits the room temperature Raman spectrum for the $Zn_{0.94}Er_{0.02}Cr_{0.04}O$ compound. For ZnO with the hexagonal wurtzite structure, the optical mode frequencies of the Brillouin zone are in the region between 99 and 600 cm^{-1} [41–45]. The $E_2^{(low)}$ and $B_1^{(low)}$ modes emerge in the low frequency regions (100 cm^{-1} and 275 cm^{-1}, respectively); the $E_2^{(high)}$, $E_1(TO)$ and $A_1(TO)$ are found at frequency zones between 370 cm^{-1} and 440 cm^{-1}; while for higher frequencies (500 cm^{-1} to 700 cm^{-1}) the $E_1(LO)$, $A_1(LO)$ and $B_1^{(high)}$ modes are more common [41–45]. For the compound under study, the $E_2^{(Low)}$ mode is present at the frequency of 99 cm^{-1}, the $E_2^{(high)} - E_2^{(low)}$ modes emerge as a shoulder at

331 cm^{-1} while an intense peak located at 437 cm^{-1} belongs to the E$_2^{(high)}$ mode [43,45]. In Figure 1b, a broad peak centered at 294 cm^{-1} is noted. According to the literature, the B$_1^{(low)}$ mode emerges at approximately 275 cm^{-1} and is related to the structural defects of Zn atoms located in neighboring interstitial sites and oxygen vacancies [41–45]. The shift to higher frequencies (294 cm^{-1}) can be attributed to an increasing number of defects due to the Er and Cr cations' inclusion in the structure, since they have distinct characteristics in relation to Zn cations (Er^{3+} (0.89 Å), Cr^{3+} (0.62 Å) and Zn^{2+} (0.74Å)) [38]. For the region between 500 and 700 cm^{-1}, the emergence of E$_1$(LO), A$_1$(LO) and B$_1^{(high)}$ modes has been reported [44,45]. In the present study, peaks appear at 501, 539, 620 and 678 cm^{-1}, which may be associated with oxygen vacancy (V$_o$) defects that arise from the difference between the oxidation states of the dopant cations and the host cation [44,45]. This conclusion is also based on the results reported by Rocha et al. [37] for pure ZnO structures, since for the region marked in Figure 1b (defect region), the authors did not observe characteristic peaks of the optical mode frequencies of the Brillouin zone for the wurtzite structure.

To attest the defects emerging from the dopant's inclusion, the PL spectrum of the Zn$_{0.94}$Er$_{0.02}$Cr$_{0.04}$O compound is measured at room temperature in the 370–750 nm range and excitation of 340 nm (Figure 2a). In Figure 2a, two well-defined peaks are observed; the first, located in the UV region and centered at 379 nm, is typical of the near-band emission (NBE) of ZnO and is related to excitonic recombination in the band gap region (between the valence and conduction bands), and the second wide peak in the visible region that is centered at 635 nm is characteristic of intrinsic defects of the lattice [46–51]. The form of the peak located in the visible region confirms the degree of point defects that emerge in the compound due to the dopant's inclusion, synthesis route, pH, annealing temperature, etc. [38]. In the present study, the difference in the oxidation state of the dopant cations and the host cations, as well as their ionic radius, play the key role for the development of high defects' concentrations in the structure.

To quantify the point defects present in the hexagonal structure after the Er and Cr cations' inclusion, the PL spectrum is deconvolved using a Gaussian distribution function. The defects of V$_o$ are related to the origin of green emission; in addition, it has been shown that V$_{Zn}$ also contributes to broadband emission in the green region [46,52,53]. In our sample, the green emission centered at ~510.9 nm (2.43 eV) corresponds to V$_{Zn}$. The bands related to V$_o$ defects appear in higher wavelength regions. Commonly, the V$_o$ defects reported for ZnO nanostructures appear in three states, i.e., neutral oxygen vacancy (V$_o$), single charge (V$_o^+$) and double charge (V$_o^{++}$) [53]. Note that, in our sample, there are no defects associated with neutral oxygen vacancies (V$_o$). The yellow emission at ~573.4 nm (2.16 eV) originates from V$_o^+$ and the orange-red emission at ~639.9 nm (1.94 eV) derives from V$_o^{++}$. Finally, the peak centered in the red region at ~694.3 nm (1.79 eV) can be attributed to O$_i$ [37]. The simplified scheme of the transitions from the conduction band to the valence band is represented in Figure 2b. The defects' quantification is shown in the pie chart, presented in the inset of Figure 2a, which contains the percentage of the area under the Gaussian curve and shows the relative concentration of point defects existing in the Zn$_{0.94}$Er$_{0.02}$Cr$_{0.04}$O compound.

Note that the simply ionized (V$_o^+$ (35%)) and double ionized (V$_o^{++}$ (47%)) oxygen vacancies' defects are predominant in the compound, which is evident because divalent Zn^{2+} cations are substituted by trivalent Er^{3+} and Cr^{3+} cations. In addition, other defects that appear in the sample, but in lower concentrations, are oxygen interstitial (O$_i$ (14%)) and zinc vacancy (V$_{Zn}$ (4%)). Similar results have been reported in the literature for rare earth and transition metal-doped ZnO compounds [46–51]. On the other hand, the UV–Vis diffuse reflectance spectrum of the Zn$_{0.94}$Er$_{0.02}$Cr$_{0.04}$O compound is shown in Figure 2c. We can see three defined bands at 487, 521 and 650 nm, which certify the replacement of Zn cations by Er cations in the ZnO crystal structure. According to the literature, these bands point to the transitions from the ground level (^{4}I$_{15/2}$) to the excited states (^{4}F$_{5/2}$), (^{4}F$_{7/2}$) and (^{4}F$_{9/2}$) when dopant Er cations are inserted into the hexagonal structure [54]. Using the Kubelka–Munk model and Tauc's plot, the band gap energy of the compound is

estimated (Figure 2d) [55]. The calculated value (3.323 ± 0.001 eV) is in agreement with the value reported for ZnO bulk (3.35 eV) [49]. However, a comparison with the value reported by Rocha et al. [37] indicates that the Er and Cr inclusion in the ZnO host lattice can cause an energetic competition, which allows the Fermi level to move for the conduction band, increasing the concentration of carriers and causing an increase in the optical gap [56]. Similar results have been observed by different authors for doped ZnO structures [49,56].
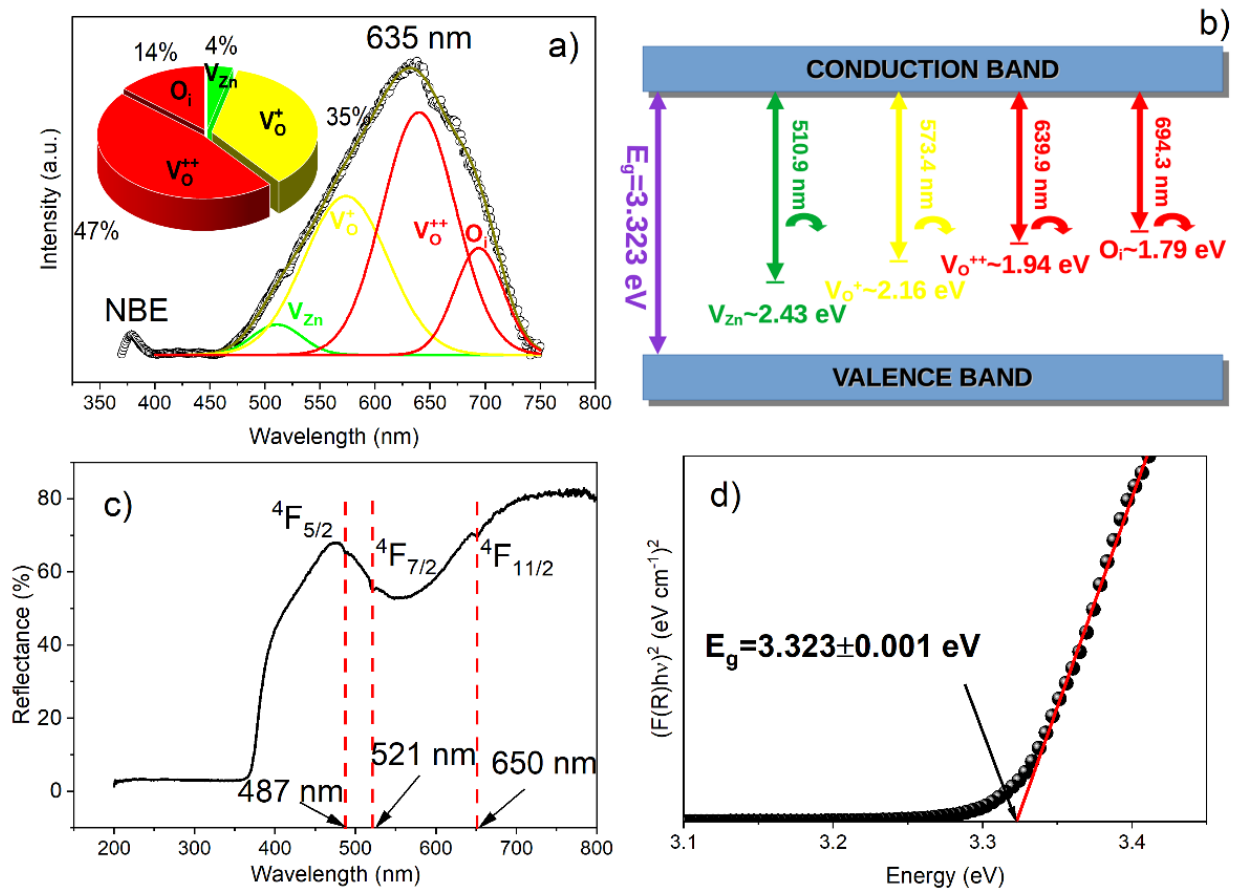
Figure 2. (**a**) PL spectrum at room temperature, (**b**) PL spectrum deconvolution, (**c**) diffuse reflectance spectrum and (**d**) optical band gap. The inset of (**b**) displays the pie charts of the relative percentage of defects for the $Zn_{0.94}Er_{0.02}Cr_{0.04}O$ compound.

The morphology of the $Zn_{0.94}Er_{0.02}Cr_{0.04}O$ compound was studied by SEM and the image is shown in Figure 3a. As observed, the sample presents agglomerates of hemisphere-like particles with sizes between 80 to 100 nm, being in the order of the crystallite sizes calculated from the Scherrer equation (86 nm).

Different morphologies have been obtained for the ZnO compound (flowers, rods, disks, hexagons, etc.), which are highly reliant on pH, temperature and synthesis methods [32,57–59]; however, hemisphere-like structures are not very common, which leads us to assume that there is a solid influence of Er^{3+} and Cr^{3+} cations on the ZnO morphology, possibly favoring the nucleation and growth mechanisms. Finally, Figure 3b shows the EDS spectrum of the compound $Zn_{0.94}Er_{0.02}Cr_{0.04}O$, where characteristic peaks of the Zn, O, Er and Cr elements can be observed, which certify the hexagonal structure formation, as well as the replacement of Zn^{2+} cations by Er^{3+} and Cr^{3+} cations in the host lattice. The peaks of Au and C elements are characteristic of the sample coating and sample holder, respectively.
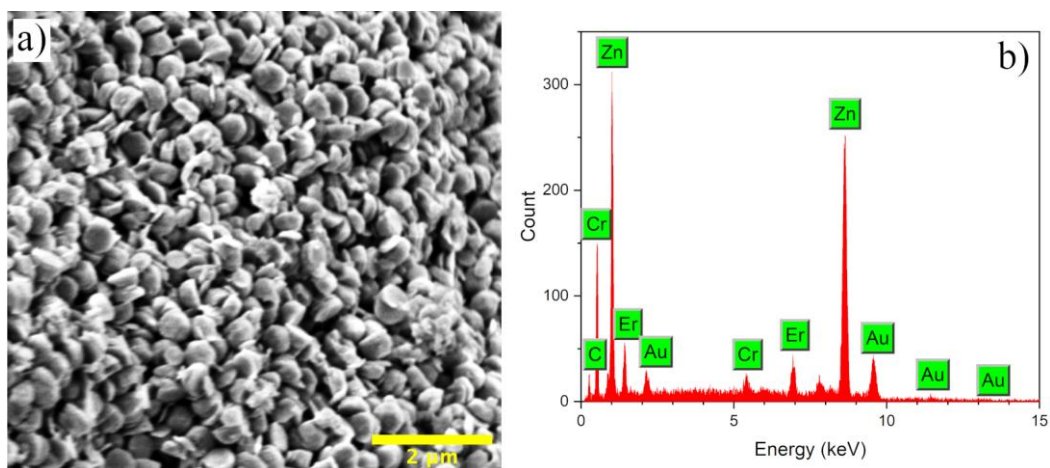
Figure 3. (**a**) SEM image and (**b**) EDS spectrum of the $Zn_{0.94}Er_{0.02}Cr_{0.04}O$ compound synthetized by co-precipitation.

3.2. Photocatalytic Performance

The photocatalytic response of the $Zn_{0.94}Er_{0.02}Cr_{0.04}O$ using an MB dye contaminant is presented in Figure 4. According to the absorption spectra (Figure 4a), the absorption maximum at 664 nm decreases during system irradiation, that can be attributed to dye degradation reactions mediated by the material synthesized. In addition, the increase in the absorption in the region between 400 and 525 nm is associated to the formation of photoproducts that absorb in this region [57,60,61]. After 150 min, the MB degradation rate is found to be 42.3%. On the other hand, in the photolysis test, the MB degradation is ~10.60%.
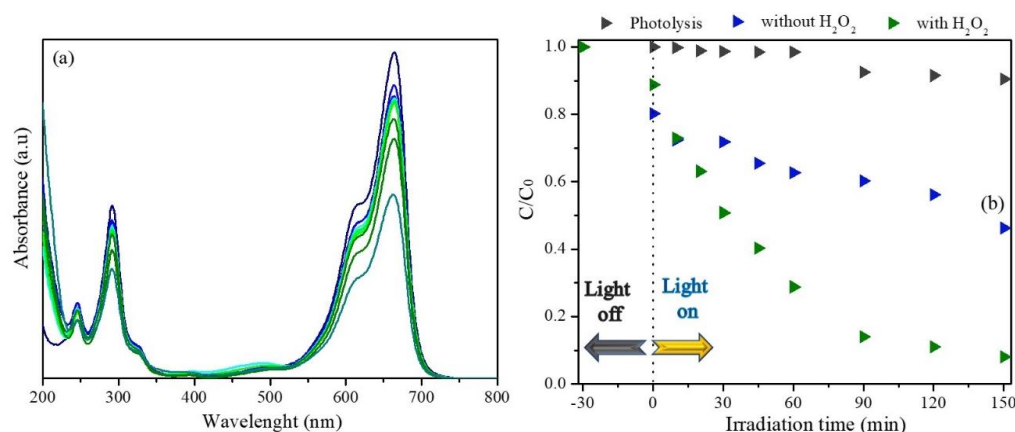

Figure 4. Photocatalytic study of $Zn_{0.94}Er_{0.02}Cr_{0.04}O$ sample: (**a**) spectral variation and (**b**) C/C_0 ratio comparative of the photocatalytic system with and without H_2O_2 as a function of irradiation time.

To optimize the photocatalytic response of the $Zn_{0.94}Er_{0.02}Cr_{0.04}O$ material, 100 ppm at H_2O_2 is added to the reaction medium. This concentration is used based on previous descriptions in the literature that consider it adequate for semiconductor ZnO photocatalytic processes [35]. In this condition, the dye removal capacity is 90.1%. The addition of H_2O_2 in the heterogeneous photocatalysis increases the organic pollutant degradation rate, because H_2O_2 can capture the photogenerated electrons efficiently and delay the recombination of the electron/hole pair [62].

Scavenger tests are performed to determine the contribution of species involved in the degradation of MB by the $Zn_{0.94}Er_{0.02}Cr_{0.04}O$ photocatalyst, and the results are displayed in Figure 5. The degradation rate of MB is 1.7%, 24.0% and 84.8% in tests using MetOH, EDTA and $AgNO_3$ as scavengers, respectively. As seen, the MB removal is drastically

affected when MetOH is added to the photocatalytic system. This reagent is well reported in the literature for capturing $^\bullet$OH radicals in the photocatalytic medium. Thus, this result suggests that $^\bullet$OH radicals are directly involved in the photocatalytic activity of $Zn_{0.94}Er_{0.02}Cr_{0.04}O$. Using EDTA, that is a hole scavenger, the dye removal capacity also increases, indicating that these species also participate in the photocatalytic activity of the semiconductor.
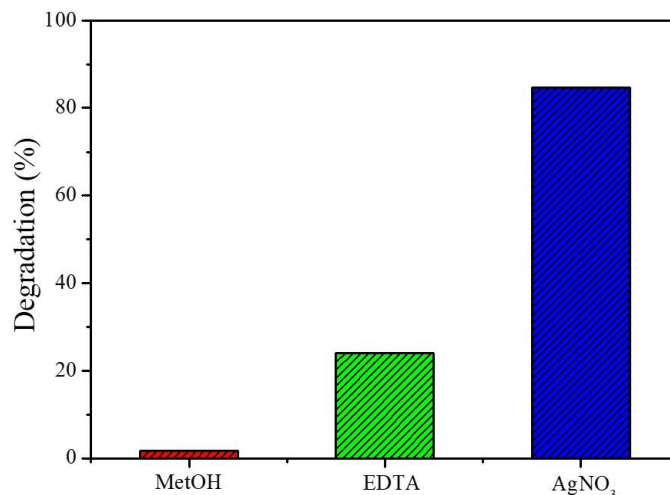

Figure 5. Photocatalytic systems containing different inhibitor reagents.

Interestingly, the rate of dye degradation increases when $AgNO_3$ is added to the reaction medium. This reagent captures electrons from the conduction band and the recombination of the e^-/h^+ pair is difficult, favoring the photocatalytic reactions. Sá et al. (2021) reported similar results and attributed them to the electron capture by Ag^0 deposited on the semiconductor surface [63]. Based on these results, a brief mechanism involved in photocatalysis of the $Zn_{0.94}Er_{0.02}Cr_{0.04}O$ sample is illustrated in Figure 6. When the $Zn_{0.94}Er_{0.02}Cr_{0.04}O$ compound absorbs a photon of energy, the charge carrier's electrons (e^-) and holes (h^+) are formed in the conduction (BC) and valence (VB) bands, respectively. These charges react with molecular species adsorbed on the semiconductor surface. Different reactions at the solid–liquid interface cause the formation of $^\bullet$OH radicals that are important to react with the structure of the pollutant forming intermediate photoproducts.
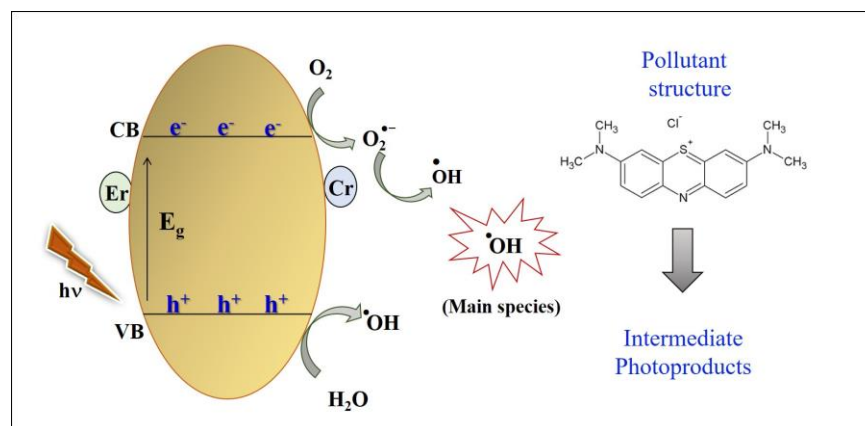

Figure 6. Photocatalytic mechanism of $Zn_{0.94}Er_{0.02}Cr_{0.04}O$ material.

The MB dye solution irradiated with the sample obtained in this study is investigated from the ecotoxicity assay using *Artemia salina*. It is known that during the photodegradation of dyes, the intermediates formed can be more toxic than the dye itself [64]. As *A.*

salina are microcrustaceans sensitive to the presence of contaminants, the test is efficient to verify the toxicity of intermediates formed in the photocatalytic process [65]. The results are expressed in terms of nauplii survival after 24 and 48 h of contact with the irradiated solution and are shown in Figure 7. Observing the results, at both investigation times, the survival rate of microcrustaceans is lower than the control group. However, these values are greater than 50%, indicating that the intermediate photoproducts are not toxic [66].
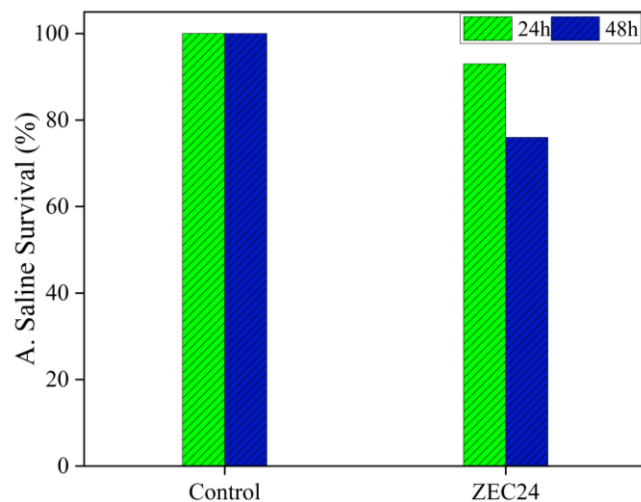
Figure 7. Ecotoxicity essay using *Artemia salina*.

Photocatalyst recycling is considered for three consecutive cycles in this study. As shown in Figure 8, the MB removal capacity decreases after the second reuse, in which a degradation rate of 23.3% is observed. In the third reuse, the photocatalytic response of the material is 21.3%. The decrease in the rate of degradation in reuse cycles can occur due to mass loss and the photocorrosion process of the ZnO when subjected to UV radiation [14,32].
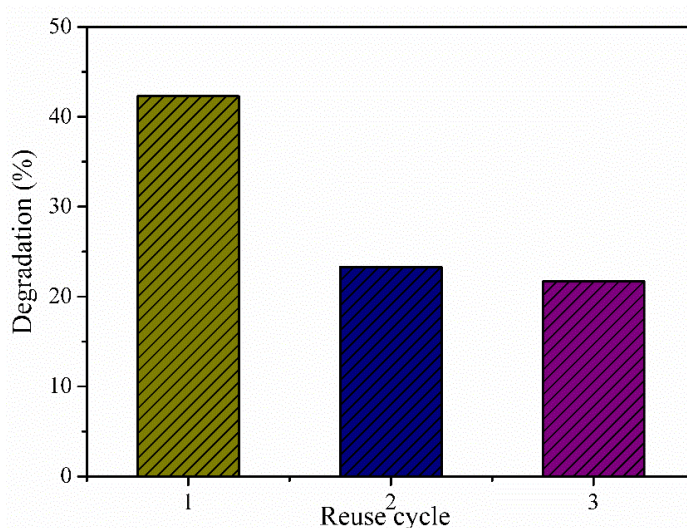

Figure 8. Reuse of $Zn_{0.94}Er_{0.02}Cr_{0.04}O$ for photocatalysis in three consecutive cycles.

4. Conclusions

The $Zn_{0.94}Er_{0.02}Cr_{0.04}O$ compound with a hemisphere-like structure was successfully obtained using the co-precipitation method. Secondary phases of the dopant cations were not identified, suggesting that the concentrations of dopants used did not exceed the solubility limit in the ZnO lattice. The predominance of oxygen vacancies confirmed by the

PL spectrum deconvolution suggests that dopant cations occupied the position of the Zn cations in the ZnO crystal structure. However, the differences between the ionic radii of the dopant species, in relation to the Zn cation, caused a lattice contraction. MB removal occurred due to mechanisms involving $^\bullet$OH radicals. These species are very efficient to degrade organic molecules, generating non-toxic photoproducts. Under optimized conditions, it is possible to potentiate the photocatalytic activity of $Zn_{0.94}Er_{0.02}Cr_{0.04}O$. Finally, this study suggests that the ZnO co-doped with Er^{3+} and Cr^{3+} can be strategically beneficial for removing pollutants via photocatalysis.

References

1. Hamadani, H.; Rashid, S.M.; Rehman, M.U.; Ali, R.; Rashid, M.; Rahman, M.; Hussain, I.; Gul, G.; ul Haq, Z. Global scenario of remediation techniques to combat environmental pollution. In *Bioremediation and Biotechnology*; Springer: Cham, Switzerland, 2020; ISBN 9783030356910.
2. Ayub, A.; Irfan, A.; Raza, Z.A.; Abbas, M.; Muhammad, A.; Ahmad, K.; Munwar, A. Development of Poly(1-Vinylimidazole)-Chitosan Composite Sorbent under Microwave Irradiation for Enhanced Uptake of Cd(II) Ions from Aqueous Media. *Polym. Bull.* **2022**, *79*, 807–827. [CrossRef]
3. Sanakousar, F.M.; Vidyasagar, C.; Jiménez-Pérez, V.M.; Prakash, K. Recent Progress on Visible-Light-Driven Metal and Non-Metal Doped ZnO Nanostructures for Photocatalytic Degradation of Organic Pollutants. *Mater. Sci. Semicond. Process.* **2022**, *140*, 106390. [CrossRef]
4. Honorio, L.M.C.; Trigueiro, P.A.; Viana, B.C.; Ribeiro, A.B.; Osajima, J.A. *Nanostructured Materials for the Photocatalytic Degradation of Organic Pollutants in Water*; Springer: Cham, Switzerland, 2019; ISBN 9783030337445.
5. Kabra, K.; Chaudhary, R.; Sawhney, R.L. Treatment of Hazardous Organic and Inorganic Compounds through Aqueous-Phase Photocatalysis: A Review. *Ind. Eng. Chem. Res.* **2004**, *43*, 7683–7696. [CrossRef]
6. Wang, J.L.; Xu, L.J. Advanced Oxidation Processes for Wastewater Treatment: Formation of Hydroxyl Radical and Application. *Crit. Rev. Environ. Sci. Technol.* **2012**, *42*, 251–325. [CrossRef]
7. De Araújo, K.S.; Antonelli, R.; Gaydeczka, B.; Granato, A.C.; Malpass, G.R.P. Advanced Oxidation Processes: A Review Regarding the Fundamentals and Applications in Wastewater Treatment and Industrial Wastewater. *Ambiente Agua-Interdiscip. J. Appl. Sci.* **2016**, *11*, 387–401. [CrossRef]
8. Chen, D.; Cheng, Y.; Zhou, N.; Chen, P.; Wang, Y.; Li, K.; Huo, S.; Cheng, P.; Peng, P.; Zhang, R.; et al. Photocatalytic Degradation of Organic Pollutants Using TiO$_2$-Based Photocatalysts: A Review. *J. Clean. Prod.* **2020**, *268*, 121725. [CrossRef]
9. Byrne, C.; Subramanian, G.; Pillai, S.C. Recent Advances in Photocatalysis for Environmental Applications. *J. Environ. Chem. Eng.* **2017**, *6*, 3531–3555. [CrossRef]

10. Morais, A.I.S.; Oliveira, W.V.; Oliveira, V.V.; Araujo, F.P.; Bezerra, R.D.S.; Fechine, P.B.A.; Viana, B.C.; Furtini, M.B.; Silva-filho, E.C.; Osajima, J.A. Semiconductor Supported by Palygorskite and Layered Double Hydroxides Clays to Dye Discoloration in Solution by a Photocatalytic Process. *J. Environ. Chem. Eng.* **2019**, *7*, 103431. [CrossRef]

11. Serpone, N.; Emeline, A.V. Semiconductor Photocatalysis—Past, Present, and Future Outlook. *J. Phys. Chem. Lett.* **2012**, *3*, 673–677. [CrossRef]

12. Maynez-Navarro, O.D.; Sánchez-Salas, J.L. Focus on Zinc Oxide as a Photocatalytic Material for Water Treatment. *Int. J. Bioremediat. Biodegrad.* **2018**, *106*. [CrossRef]

13. Moosavi, F.; Bahrololoom, M.E.; Kamjou, R. Influence of Pb and Co-Doping on Photocatalytic Degradation Performance of ZnO Thin Films. *J. Ultrafine Grained Nanostruct. Mater.* **2021**, *54*, 173–179. [CrossRef]

14. Lemos, S.C.S.; de Lima Rezende, T.K.; Assis, M.; da Costa Romeiro, F.; Peixoto, D.A.; de Oliveira Gomes, E.; Jacobsen, G.M.; Teodoro, M.D.; Gracia, L.; Ferrari, J.L.; et al. Efficient Ni and Fe Doping Process in ZnO with Enhanced Photocatalytic Activity: A Theoretical and Experimental Investigation. *Mater. Res. Bull.* **2022**, *152*, 111849. [CrossRef]

15. Araujo, F.P.; Trigueiro, P.; Honório, L.M.C.; Furtini, M.B.; Oliveirab, D.M.; Almeidac, L.C.; Garcia, R.R.P.; Viana, B.C.; Silva-Filho, E.C.; Osajima, J.A. Novel Green Approach Based on ZnO Nanoparticles and Polysaccharides for Photocatalytic Performance. *Dalton Trans.* **2020**, *49*, 16394–16403. [CrossRef] [PubMed]

16. Ong, C.B.; Ng, L.Y.; Mohammad, A.W. A Review of ZnO Nanoparticles as Solar Photocatalysts: Synthesis, Mechanisms and Applications. *Renew. Sustain. Energy Rev.* **2018**, *81*, 536–551. [CrossRef]

17. Truong, T.K.; Van Doan, T.; Tran, H.H.; Van Le, H.; Lam, V.Q.; Tran, H.N.; Cao, T.M.; Van Pham, V. Effect of Cr Doping on Visible-Light-Driven Photocatalytic Activity of ZnO Nanoparticles. *J. Electron. Mater.* **2019**, *48*, 7378–7388. [CrossRef]

18. Ahmad, I.; Shoaib Akhtar, M.; Ahmed, E.; Ahmad, M.; Keller, V.; Qamar Khan, W.; Khalid, N.R. Rare Earth Co-Doped ZnO Photocatalysts: Solution Combustion Synthesis and Environmental Applications. *Sep. Purif. Technol.* **2020**, *237*, 116328. [CrossRef]

19. Devi, K.N.; Devi, S.A.; Singh, W.J.; Singh, K.J. Nickel Doped Zinc Oxide with Improved Photocatalytic Activity for Malachite Green Dye Degradation and Parameters Affecting the Degradation. *J. Mater. Sci. Mater. Electron.* **2021**, *32*, 8733–8745. [CrossRef]

20. Kannadasan, N.; Shanmugam, N.; Cholan, S.; Sathishkumar, K.; Viruthagiri, G.; Poonguzhali, R. The Effect of Ce^{4+} Incorporation on Structural, Morphological and Photocatalytic Characters of ZnO Nanoparticles. *Mater. Charact.* **2014**, *97*, 37–46. [CrossRef]

21. Tang, L.; Jia, Y.; Zhu, Z.; Hua, Y.; Wu, J.; Zou, Z.; Zhou, Y. Effects of Co Doping on the Growth and Photocatalytic Properties of ZnO Particles. *Molecules* **2022**, *27*, 833. [CrossRef]

22. Abdel Messih, M.F.; Ahmed, M.A.; Soltan, A.; Anis, S.S. Synthesis and Characterization of Novel Ag/ZnO Nanoparticles for Photocatalytic Degradation of Methylene Blue under UV and Solar Irradiation. *J. Phys. Chem. Solids* **2019**, *135*, 109086. [CrossRef]

23. Kaneva, N.V.; Dimitrov, D.T.; Dushkin, C.D. Effect of Nickel Doping on the Photocatalytic Activity of ZnO Thin Films under UV and Visible Light. *Appl. Surf. Sci.* **2011**, *257*, 8113–8120. [CrossRef]

24. Mittal, M.; Sharma, M.; Pandey, O.P. UV-Visible Light Induced Photocatalytic Studies of Cu Doped ZnO Nanoparticles Prepared by Co-Precipitation Method. *Sol. Energy* **2014**, *110*, 386–397. [CrossRef]

25. Biswas, B.D.; Purkayastha, M.D.; Tiwari, E.; Denrah, S.; Sarkar, M.; Darbha, G.K.; Majumder, T.P. Study of the Photocatalytic Activity of Mn-Doped ZnO Nanocomposites Depending on Their Morphology and Structure with the Variation of Manganese Concentration. *Surf. Interfaces* **2021**, *23*, 100902. [CrossRef]

26. Alkallas, F.H.; Trabelsi, A.B.G.; Nasser, R.; Fernandez, S.; Song, J.M.; Elhouichet, H. Promising Cr-Doped ZnO Nanorods for Photocatalytic Degradation Facing Pollution. *Appl. Sci.* **2022**, *12*, 34. [CrossRef]

27. Akhtar, J.; Tahir, M.B.; Sagir, M.; Bamufleh, H.S. Improved Photocatalytic Performance of Gd and Nd Co-Doped ZnO Nanorods for the Degradation of Methylene Blue. *Ceram. Int.* **2020**, *46*, 11955–11961. [CrossRef]

28. Kumar, R.; Dosanjh, H.S. A Mini-Review on Rare Earth Metal Doped ZnO Nanomaterials for Photocatalytic Remediation of Waste Water. *J. Phys. Conf. Ser.* **2022**, *2267*, 012139. [CrossRef]

29. Alam, U.; Khan, A.; Ali, D.; Bahnemann, D.; Muneer, M. Comparative Photocatalytic Activity of Sol-Gel Derived Rare Earth Metal (La, Nd, Sm and Dy)-Doped ZnO Photocatalysts for Degradation of Dyes. *RSC Adv.* **2018**, *8*, 17582–17594. [CrossRef]

30. Sowik, J.; Miodyńska, M.; Bajorowicz, B.; Mikolajczyk, A.; Lisowski, W.; Klimczuk, T.; Kaczor, D.; Zaleska Medynska, A.; Malankowska, A. Optical and Photocatalytic Properties of Rare Earth Metal-Modified ZnO Quantum Dots. *Appl. Surf. Sci.* **2019**, *464*, 651–663. [CrossRef]

31. Pascariu, P.; Cojocaru, C.; Olaru, N.; Samoila, P.; Airinei, A.; Ignat, M.; Sacarescu, L.; Timpu, D. Novel Rare Earth (RE-La, Er, Sm) Metal Doped ZnO Photocatalysts for Degradation of Congo-Red Dye: Synthesis, Characterization and Kinetic Studies. *J. Environ. Manag.* **2019**, *239*, 225–234. [CrossRef]

32. Costa-Silva, M.; Araujo, F.P.; Guerra, Y.; Viana, B.C.; Silva-Filho, E.C.; Osajima, J.A.; Almeida, L.C.; Skovroinski, E.; Peña-Garcia, R. Photocatalytic, Structural and Optical Properties of Ce–Ni Co-Doped ZnO Nanodisks-like Self-Assembled Structures. *Mater. Chem. Phys.* **2022**, *292*, 126814. [CrossRef]

33. Ghomri, R.; Shaikh, M.N.; Ahmed, M.I.; Bououdina, M.; Ghers, M. (Al, Er) Co-Doped ZnO Nanoparticles for Photodegradation of Rhodamine Blue. *Appl. Phys. A* **2016**, *122*, 1–9. [CrossRef]

34. Irtiqa, S.; Rahman, A. Photocatalytic Studies of La,Ce Co-Doped ZnO Nanoparticles. *Russ. J. Appl. Chem.* **2020**, *93*, 1906–1919. [CrossRef]

35. Asgari, E.; Sheikhmohammadi, A.; Manshouri, M.; Hashemzadeh, B. The Investigation of Removal Performances of UV/ZnO, UV/ZnO/H$_2$O$_2$ and UV/ZnO/O$_3$ Processes in the Degradation of Butoben and Phenylmethyl Ester from Aqueous Solution. *Optik* **2021**, *228*, 166208. [CrossRef]

36. Castro-Lopes, S.; Guerra, Y.; Silva-Sousa, A.; Oliveira, D.M.; Gonçalves, L.A.P.; Franco, A.; Padrón-Hernández, E.; Peña-Garcia, R. Influence of PH on the Structural and Magnetic Properties of Fe-Doped ZnO Nanoparticles Synthesized by Sol Gel Method. *Solid State Sci.* **2020**, *109*, 106438. [CrossRef]

37. Rocha, M.; Araujo, F.P.; Castro-Lopes, S.; de Lima, I.S.; Silva-Filho, E.C.; Osajima, J.A.; Oliveira, C.S.; Viana, B.C.; Almeida, L.C.; Guerra, Y.; et al. Synthesis of Fe–Pr Co-Doped ZnO Nanoparticles: Structural, Optical and Antibacterial Properties. *Ceram. Int.* **2023**, *49*, 2282–2295. [CrossRef]

38. Shannon, R.D. Revised Effective Ionic Radii and Systematic Studies of Interatomic Distances in Halides and Chalcogenides. *Acta Crystallogr.* **1976**, *32*, 751–767. [CrossRef]

39. Peña-Garcia, R.; Guerra, Y.; Milani, R.; Oliveira, D.M.; Rodrigues, A.R.; Padrón-Hernández, E. The Role of Y on the Structural, Magnetic and Optical Properties of Fe-Doped ZnO Nanoparticles Synthesized by Sol Gel Method. *J. Magn. Magn. Mater.* **2020**, *498*, 166085. [CrossRef]

40. Peña-Garcia, R.; Guerra, Y.; Milani, R.; Oliveira, D.M.; de Souza, F.R.; Padrón-Hernández, E. Influence of Ni and Sr on the Structural, Morphological and Optical Properties of ZnO Synthesized by Sol Gel. *Opt. Mater.* **2019**, *98*, 109427. [CrossRef]

41. Fifere, N.; Airinei, A.; Timpu, D.; Rotaru, A.; Sacarescu, L.; Ursu, L. New Insights into Structural and Magnetic Properties of Ce Doped ZnO Nanoparticles. *J. Alloys Compd.* **2018**, *757*, 60–69. [CrossRef]

42. Chen, K.J.; Fang, T.H.; Hung, F.Y.; Ji, L.W.; Chang, S.J.; Young, S.J.; Hsiao, Y.J. The Crystallization and Physical Properties of Al-Doped ZnO Nanoparticles. *Appl. Surf. Sci.* **2008**, *254*, 5791–5795. [CrossRef]

43. Song, Y.; Zhang, S.; Zhang, C.; Yang, Y.; Lv, K. Raman Spectra and Microstructure of Zinc Oxide Irradiated with Swift Heavy Ion. *Crystals* **2019**, *9*, 395. [CrossRef]

44. da Trindade, L.G.; Minervino, G.B.; Trench, A.B.; Carvalho, M.H.; Assis, M.; Li, M.S.; de Oliveira, A.J.A.; Pereira, E.C.; Mazzo, T.M.; Longo, E. Influence of Ionic Liquid on the Photoelectrochemical Properties of ZnO Particles. *Ceram. Int.* **2018**, *44*, 10393–10401. [CrossRef]

45. Musa, I.; Qamhieh, N.; Mahmoud, S.T. Synthesis and Length Dependent Photoluminescence Property of Zinc Oxide Nanorods. *Results Phys.* **2017**, *7*, 3552–3556. [CrossRef]

46. Punia, K.; Lal, G.; Alvi, P.A.; Dolia, S.N.; Dalela, S.; Modi, K.B.; Kumar, S. A Comparative Study on the Influence of Monovalent, Divalent and Trivalent Doping on the Structural, Optical and Photoluminescence Properties of Zn$_{0.96}$T$_{0.04}$O (T: Li+, Ca^{2+} & Gd^{3+}) Nanoparticles. *Ceram. Int.* **2019**, *45*, 13472–13483.

47. Poornaprakash, B.; Chalapathi, U.; Reddy, B.P.; Poojitha, P.T.; Park, S. Enhanced Ferromagnetism in ZnGdO Nanoparticles Induced by Al Co-Doping. *J. Alloys Compd.* **2017**, *705*, 51–57. [CrossRef]

48. Punia, K.; Lal, G.; Dalela, S.; Dolia, S.N.; Alvi, P.A.; Barbar, S.K.; Modi, K.B.; Kumar, S. A Comprehensive Study on the Impact of Gd Substitution on Structural, Optical and Magnetic Properties of ZnO Nanocrystals. *J. Alloys Compd.* **2021**, *868*, 159142. [CrossRef]

49. Punia, K.; Lal, G.; Barbar, S.K.; Dolia, S.N.; Alvi, P.A.; Dalela, S.; Kumar, S. Oxygen Vacancies Mediated Cooperative Magnetism in ZnO Nanocrystals: A D0 Ferromagnetic Case Study. *Vaccum* **2021**, *184*, 109921. [CrossRef]

50. Kumar, J.; Sharma, A.; Won, S.O.; Kumar, R.; Chae, K.H.; Kumar, S.; Vij, A. Probing Defects and Electronic Structure of Eu Doped T-Mg$_2$B$_2$O$_5$ Nanocrystals Using X-ray Absorption near Edge Spectroscopy and Luminescence Techniques. *Vacuum* **2020**, *180*, 7–12. [CrossRef]

51. Ma, X.; Wang, Z. The Optical Properties of Rare Earth Gd Doped ZnO Nanocrystals. *Mater. Sci. Semicond. Process.* **2012**, *15*, 227–231. [CrossRef]

52. Mhlongo, G.H.; Shingange, K.; Tshabalala, Z.P.; Dhonge, B.P.; Mahmoud, F.A.; Mwakikunga, B.W.; Motaung, D.E. Room Temperature Ferromagnetism and Gas Sensing in ZnO Nanostructures: Influence of Intrinsic Defects and Mn, Co, Cu Doping. *Appl. Surf. Sci.* **2016**, *390*, 804–815. [CrossRef]

53. Galdámez-Martinez, A.; Santana, G.; Güell, F.; Martínez-Alanis, P.R.; Dutt, A. Photoluminescence of Zno Nanowires: A Review. *Nanomaterials* **2020**, *10*, 857. [CrossRef]

54. Jayachandraiah, C.; Krishnaiah, G. Erbium Induced Raman Studies and Dielectric Properties of Er-Doped ZnO Nanoparticles. *Adv. Mater. Lett.* **2015**, *6*, 743–748. [CrossRef]

55. Soares, A.S.S.; Castro-Lopes, S.; Cabrera-Baez, M.; Milani, R.; Padrón-Hernández, E.; Farias, B.V.V.; Soares, J.M.; Gusmão, S.S.; Viana, B.C.; Guerra, Y.; et al. The Role of PH on the Vibrational, Optical and Electronic Properties of the Zn FeO Compound Synthesized via Sol Gel Method. *Solid State Sci.* **2022**, *128*, 106880. [CrossRef]

56. Mondal, S.; Bhattacharyya, S.R.; Mitra, P. Effect of Al Doping on Microstructure and Optical Band Gap of ZnO Thin Film Synthesized by Successive Ion Layer Adsorption and Reaction. *Pramana-J. Phys.* **2013**, *80*, 315–326. [CrossRef]

57. Araujo, F.P.; Trigueiro, P.; Honório, L.M.C.; Oliveira, D.M.; Almeida, L.C.; Garcia, R.P.; Lobo, A.O.; Cantanhêde, W.; Silva-Filho, E.C.; Osajima, J.A. Eco-Friendly Synthesis and Photocatalytic Application of Flowers-like ZnO Structures Using Arabic and Karaya Gums. *Int. J. Biol. Macromol.* **2020**, *165*, 2813–2822. [CrossRef]

58. Akhir, R.M.; Harrum, W.M.W.; Buniyamin, I.; Rusop, M.; Khusaimi, Z. Enhanced Structural and Morphological Properties of ZnO Nanorods Using Plant Extract-Assisted Solution Immersion Method. *Mater. Today Proc.* **2021**, *48*, 1855–1860. [CrossRef]

59. Trung, D.Q.; Tran, M.T.; Tu, N.; Thu, L.T.H.; Huyen, N.T.; Hung, N.D.; Viet, D.X.; Kien, N.D.T.; Huy, P.T. Synthesis, Structural and Optical Properties of ZnS/ZnO Heterostructure-Alloy Hexagonal Micropyramids. *Opt. Mater.* **2022**, *125*, 112077. [CrossRef]

60. Fe, S. Visible Photocatalytic Degradation of Methylene Blue on Magnetic. *J. Mater. Sci. Mater. Electron.* **2018**, *123*, 157–161. [CrossRef]

61. Matsunami, D.; Yamanaka, K.; Mizoguchi, T.; Kojima, K. Comparison of Photodegradation of Methylene Blue Using Various TiO_2 Films and WO_3 Powders under Ultraviolet and Visible-Light Irradiation. *J. Photochem. Photobiol. A Chem.* **2019**, *369*, 106–114. [CrossRef]

62. Navarro, S.; Fenoll, J.; Vela, N.; Ruiz, E.; Navarro, G. Photocatalytic Degradation of Eight Pesticides in Leaching Water by Use of ZnO under Natural Sunlight. *J. Hazard. Mater.* **2009**, *172*, 1303–1310. [CrossRef] [PubMed]

63. Sá, A.S.; Feitosa, R.P.; Honório, L.; Peña-Garcia, R.; Almeida, L.C.; Dias, J.S.; Brazuna, L.P.; Tabuti, T.G.; Triboni, E.R.; Osajima, J.A.; et al. A Brief Photocatalytic Study of Zno Containing Cerium towards Ibuprofen Degradation. *Materials* **2021**, *14*, 5891. [CrossRef]

64. Konstantinou, I.K.; Albanis, T.A. TiO_2-Assisted Photocatalytic Degradation of Azo Dyes in Aqueous Solution: Kinetic and Mechanistic Investigations: A Review. *Appl. Catal. B Environ.* **2004**, *49*, 1–14. [CrossRef]

65. Selvinsimpson, S.; Eva Gnana Dhana Rani, S.; Ganesh Kumar, A.; Rajaram, R.; Sharmila Lydia, I.; Chen, Y. Photocatalytic Activity of SnO_2/Fe_3O_4 Nanocomposites and the Toxicity Assessment of Vigna Radiata, Artemia Salina and Danio Rerio in the Photodegraded Solution. *Environ. Res.* **2021**, *195*, 110787. [CrossRef]

66. Souza, R.P.; Freitas, T.K.F.S.; Domingues, F.S.; Pezoti, O.; Ambrosio, E.; Ferrari-Lima, A.M.; Garcia, J.C. Photocatalytic Activity of TiO_2, ZnO and Nb_2O_5 Applied to Degradation of Textile Wastewater. *J. Photochem. Photobiol. A Chem.* **2016**, *329*, 9–17. [CrossRef]